sciendo
Control and Cybernetics
vol. **53** (2024) No. 1
pages: 109-140
DOI: 10.2478/candc-2024-0006

2D mechanical metamaterials synthesized by topology optimization in the different symmetry classes*

by

Xuan-Nam Do[1], Valentin Calisti[2,*] and Jean-François Ganghoffer[1,*]

[1] LEM3, Université de Lorraine, CNRS. Arts et Métiers Paris Tech. 7, rue Félix Savart, 57073, Metz, France
jean-francois.ganghoffer@univ-lorraine.fr
[2] Institute of Mathematics of the Czech Academy of Sciences
Žitná 25, 115 67 Praha 1, Czech Republic
calistivalentin@gmail.com
* corresponding author

Abstract: The aim of this paper is to recourse to topology optimization method to synthesize mechanical matematerials, based on the topologial derivative. Material symmetries play a major role in the very definition and expression of the homogenized properties; the search of optimal microstructures is done in given symmetry classes characterized by invariants of the homogenized moduli. We synthesize thanks to this methodology periodic microstructures prone to auxetic and anti-auxetic behaviors, or with a very large or small bulk to shear modulus ratio.

Keywords: mechanical metamaterials, architected materials, topology optimization, material symmetries, auxetic materials

1. Introduction

The rise of additive manufacturing, alongside advancements in engineering analysis tools, has heralded a new era in design, emphasizing deliberate manipulation of material organization. This pivotal shift has spawned a revolutionary class of artificial materials known as metamaterials, distinguished by their remarkable static and dynamic properties not typically observed in natural substances (Liu et al, 2000). These properties often encompass an exceptionally high bulk-to-shear modulus ratio or a significantly negative Poisson's ratio, surpassing those of conventional materials (Bertoldi et al., 2017; Lakes, 1993). Moreover, the

*Submitted: June 2024; Accepted: August 2024.

term "metamaterials" encapsulates the fundamental principle of altering topology within a repetitive unit cell, as opposed to modifying the intrinsic properties of the base material (Smith, Pendry and Wiltshire, 2004). Thus, metamaterials in this context are defined as artificial materials, whose mechanical characteristics derive from their internal structure, meticulously engineered into periodically arranged unit cells, rather than from their chemical composition (Liu and Zhang, 2011; Wang et al., 2014).

Considerable research efforts have been dedicated to designing and analyzing auxetic metamaterials, characterized by negative Poisson's ratios (Liu and Hu, 2010). Significant studies have delved into the mechanical properties of chiral lattices, hexa- and tetrachiral cellular solids (Spadoni and Ruzzene, 2012; Bacigalupo and Gambarotta, 2014). Auxetics find applications across diverse industries such as aerospace and automotive, owing to their exceptional shear strength and reduced structural weight (Prawoto, 2012). Poisson's ratio serves as a crucial metric for assessing material performance. While isotropic materials have limited Poisson's ratio values, anisotropic materials can surpass these limits (Greaves et al., 2011). Introducing a degree of anisotropy is imperative to achieve unconventional mechanical behaviors, a recognition echoed across various engineering fields, including morphing wing applications in aerospace (Olympio and Ghandi, 2010).

Successful morphing in aerospace or wind energy engineering hinges on the utilization of materials that combine low stiffness and high Poisson's ratio in one direction to minimize actuation energy, with high stiffness in the perpendicular direction to support aerodynamic loads (Olympio and Ghandi, 2010). Certain honeycomb and hybrid accordion cellular solids fulfill these stiffness characteristics. The development of metamaterials with controlled anisotropy, tailored to be ultrasoft or ultra-stiff, while remaining lightweight, has gained significance not only in morphing applications, but also in biomechanical, civil, and mechanical engineering.

Three-dimensional unit cells have been meticulously designed to achieve specified material stiffness ratios using evolutionary structural optimization methods (Yang et al., 2013). Additionally, various cubic-shaped lattices and origami lattices have been employed to optimize bulk and shear moduli and control Young's modulus values (Silverberg et al., 2014). In addition to network materials, reinforced composite structures have attained highly anisotropic mechanical properties, with stiffness ratios between two normal material directions ranging from hundreds to thousands (Peel, 2007). These composites are poised to be utilized in the design of vibration damping or actuation devices with superior properties. Some applications necessitate anisotropic material designs, not only due to stiffness requirements, but also because of their Poisson's ratio behavior. Recently, graphene materials with near-zero Poisson's ratio values

have been fabricated, showing promise for nano-engineering applications. Moreover, specific biological structures, like tendons and ligaments exhibit Poisson's ratio values well beyond the isotropic limits (Reese, Maas and Weiss, 2010), necessitating the development of biocompatible biosubstitute materials for reconstructing injured tissues, such as ligaments and tendons to mimic the native tissue's mechanical response (see also Fig. 1).

Despite the rapid expansion of the field of mechanical metamaterials over the past two decades, the quest for their extraordinary properties still primarily relies on a heuristic approach, as observed in the literature (Bertoldi et al., 2017). However, recent advancements have seen the emergence of a few works employing topology optimization as a rational methodology for design and characterization (Mendez et al., 2019; Podestá et al., 2019; Sigmund and Mante, 2013; Rossi et al., 2020, 2021; Yera et al., 2020). In this paper, we aim to synthesize mechanical metamaterials with auxetic behavior or low or high bulk-to-shear modulus using topology optimization as a systematic methodology. A novel aspect of our work involves classifying microstructures according to their material symmetries, defined as invariants of the Cauchy homogenized moduli.

The paper is organized as follows: Section 2 outlines the classification of material symmetries based on invariants. Section 3 provides a self-contained overview of the topological optimization method using the topological derivative. Section 4 presents numerical results for minimizing Poisson's ratio across different symmetry classes in 2D and optimizing the bulk-to-shear modulus, chosen as a performance index for mechanical metamaterials. Finally, Section 5 concludes with a summary of our work and potential future developments in the field of topology optimization.

2. Classification of materials elastic behaviors in 2D based on material symmetries

2.1. Intrinsic definition of the mechanical moduli

The intrinsic definition of the mechanical moduli is based on the compliance tensor, which is the inverse of the rigidity tensor, when adopting Bechterew's basis (Bechterew, 1926). This basis is used to consistently represent the strain and stress tensors (denoted by $\underset{\approx}{\boldsymbol{\varepsilon}}$ and $\underset{\approx}{\boldsymbol{\sigma}}$, respectively) for formulating the effective constitutive law. In this basis, the tensor of effective rigidity moduli ($\underset{\approx}{\mathbf{C}}$) is represented as shown in Fig. 2. It is important to note that vectors and tensors will be written with boldface symbols. Additionally, the convention of summing repeated indices in a monomial will be systematically applied throughout this paper.

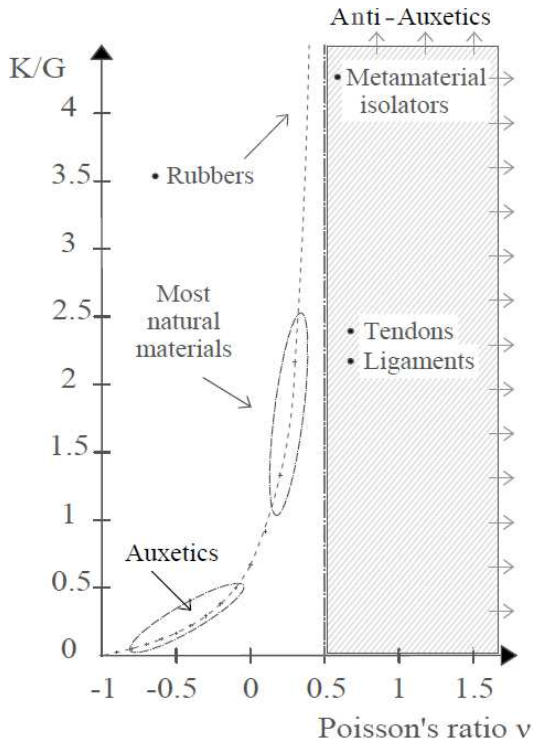

Figure 1: Auxetic and anti-auxetic materials in a diagram of the ratio of bulk to shear modulus ($\frac{K}{G}$) versus Poisson's ratio in a 3D situation

$$\underbrace{\begin{bmatrix} \sigma_{11} \\ \sigma_{22} \\ \sigma_{33} \\ \sqrt{2}\sigma_{23} \\ \sqrt{2}\sigma_{31} \\ \sqrt{2}\sigma_{12} \end{bmatrix}}_{\underline{\sigma}} = \underbrace{\begin{bmatrix} C_{1111} & C_{1122} & C_{1133} & \sqrt{2}C_{1123} & \sqrt{2}C_{1131} & \sqrt{2}C_{1112} \\ C_{2211} & C_{2222} & C_{2233} & \sqrt{2}C_{2223} & \sqrt{2}C_{2231} & \sqrt{2}C_{2212} \\ C_{3311} & C_{3322} & C_{3333} & \sqrt{2}C_{3323} & \sqrt{2}C_{3331} & \sqrt{2}C_{3312} \\ \sqrt{2}C_{2311} & \sqrt{2}C_{2322} & \sqrt{2}C_{2333} & 2C_{2323} & 2C_{2331} & 2C_{2312} \\ \sqrt{2}C_{3111} & \sqrt{2}C_{3122} & \sqrt{2}C_{3133} & 2C_{3123} & 2C_{3131} & 2C_{3112} \\ \sqrt{2}C_{1211} & \sqrt{2}C_{1222} & \sqrt{2}C_{1233} & 2C_{1223} & 2C_{1231} & 2C_{1212} \end{bmatrix}}_{\underline{\underline{C}}} . \underbrace{\begin{bmatrix} \epsilon_{11} \\ \epsilon_{22} \\ \epsilon_{33} \\ \sqrt{2}\epsilon_{23} \\ \sqrt{2}\epsilon_{31} \\ \sqrt{2}\epsilon_{12} \end{bmatrix}}_{\underline{\epsilon}}$$

Figure 2: The tensor of effective rigidity moduli in Bechterew's basis

Utilizing the compliance tensor ($\underline{\underline{\mathbf{S}}}$), which is the inverse of the previously defined rigidity tensor (Rychlewski, 1984), we can derive the intrinsic definitions of the tensile modulus, Poisson's ratio, shear modulus, and bulk modulus for any arbitrary pair of orthogonal unit directions $\underline{\mathbf{m}}$ and $\underline{\mathbf{n}}$, spanning a specified

plane of analysis, successively

$$\begin{aligned} \mathrm{E}(\underline{\mathbf{n}}) &= \frac{1}{\underline{\mathbf{n}}\cdot\underline{\mathbf{n}}\cdot\underline{\underline{\underline{\underline{\mathbf{S}}}}}\cdot\underline{\mathbf{n}}\cdot\underline{\mathbf{n}}} \\ \nu(\underline{\mathbf{n}},\underline{\mathbf{m}}) &= -\frac{\underline{\mathbf{m}}\cdot\underline{\mathbf{m}}\cdot\underline{\underline{\underline{\underline{\mathbf{S}}}}}\cdot\underline{\mathbf{m}}\cdot\underline{\mathbf{m}}}{\underline{\mathbf{n}}\cdot\underline{\mathbf{n}}\cdot\underline{\underline{\underline{\underline{\mathbf{S}}}}}\cdot\underline{\mathbf{n}}\cdot\underline{\mathbf{n}}} \\ \mu(\underline{\mathbf{m}},\underline{\mathbf{n}}) &= \frac{1}{2\underline{\mathbf{n}}\cdot\underline{\mathbf{m}}\cdot\underline{\underline{\underline{\underline{\mathbf{S}}}}}\cdot\underline{\mathbf{m}}\cdot\underline{\mathbf{n}}} \\ \mathrm{K} &= \frac{1}{\mathrm{S}_{\mathrm{iikk}}}. \end{aligned} \tag{1}$$

These effective moduli provide a comprehensive characterization of the rigidity tensor, particularly when examining three orthogonal planes in a 3D scenario (or two in 2D). Notably, Poisson's ratio emerges as an intrinsic property of all elastic materials, derived from their compliance tensor, rather than being solely a kinematic measure of the transverse deformation, experienced by a sample or a small volume of material around a given material point.

Given that microstructures typically exhibit material symmetries, these expressions of effective moduli can be tailored further, based on the specific class of symmetries considered, thereby condensing the number of strictly independent (non-zero) moduli. The objective of the next section is to delineate the structure of the compliance tensor for existing symmetry classes in a 2D scenario, aligning with our forthcoming goal of identifying optimal microstructures within specific material symmetry groups.

2.2. Material symmetry classes in 2D linear elasticity

The constitutive law, governing periodic microstructures requires determining the tensor of homogenized moduli, a process that can be streamlined by imposing constraints on the number of strictly independent coefficients. These constraints arise from considerations of material symmetries, aligned with the Curie-Neumann principle: the symmetry of the geometry implies corresponding symmetries in the effective constitutive law. In the 2D scenario, which is discussed here, the count of material symmetries and their associated rotations and reflections, which preserve the geometry, significantly simplifies, compared to the 3D case. Four symmetries are present (Verchery, 1982; Vianello, 1997; De Saxcé and Vallée, 2013) (Z_2 for general materials, or so-called digonal triclinic; D_2 for orthogonal materials; D_4 for tetragonal materials; and $O(2)$ for isotropic materials), as listed below in ascending order of their material symmetry groups. Each symmetry is linked to specific symmetry groups, both enumerated in Table 1, where $\mathbf{Q}\left(\underline{\mathbf{n}},\theta\right)$ denotes a rotation of angle θ about axis $\underline{\mathbf{n}}$, with $\underline{\mathbf{e}}_3$ repre-

senting the unit vector normal to the analysis plane. Further insights into the impact of the rotational operator $\mathbf{Q}\left(\underline{\mathbf{e}}_3, \theta\right)$ on $\underset{\approx}{\mathbf{C}}$ in Bechterew's basis can be found in the study by De Saxcé and Vallée (2013).

Name(s)	Digonal Triclinic	Orthogonal	Tetragonal	Isotropic
Class	Z_2	D_2	D_4	$O(2)$
Generators	$Q(\underline{\mathbf{e}}_3, \pi)$	$Q(\underline{\mathbf{e}}_3, \pi)$ $Q(\underline{\mathbf{e}}_1, \pi)$	$Q(\underline{\mathbf{e}}_3, \pi/2)$ $Q(\underline{\mathbf{e}}_1, \pi)$	$Q(\underline{\mathbf{e}}_3, \theta), \forall\theta$ $Q(\underline{\mathbf{e}}_1, \pi)$
Examples	Z	0	□	◯

Table 1: Symmetry classes for 2D elasticity tensors

The rigidity tensor is structured as depicted in Fig. 3, with the number of independent components indicated in the lower right corner of each elasticity tensor. Additionally, in the same Fig. 3, straight lines denote the identity of two coefficients, while $\times = \frac{C_{11}-C_{12}}{2}$.

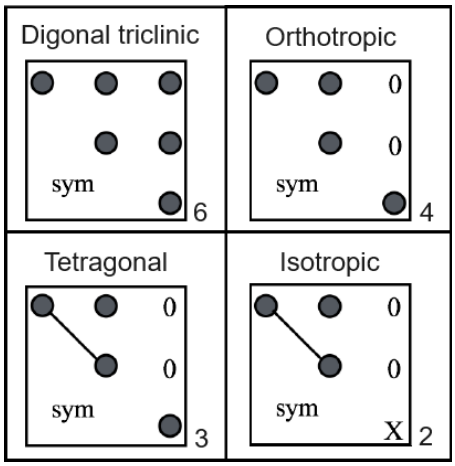

Figure 3: Structure of the rigidity tensor in 2D (non-nil coefficients) of the four material symmetry groups for 2D microstructures

The transition between symmetry classes in the preceding table is precipitated by the nullification of invariants within the rigidity tensor, depicted in Fig. 4. It is worth noting that C_{11}, C_{12}, C_{13}, C_{22}, C_{23}, and C_{33} represent the components of the homogenized elasticity tensor, as defined in Equation (4) of Section (4).

$$
\begin{aligned}
I_1 &= \frac{1}{8}\left(\mathrm{C}_{11}+\mathrm{C}_{22}+6\mathrm{C}_{12}-2\mathrm{C}_{33}\right)\\
I_2 &= \frac{1}{8}\left(\mathrm{C}_{11}+\mathrm{C}_{22}-2\mathrm{C}_{12}+2\mathrm{C}_{33}\right)\\
I_3 &= \frac{1}{2}\left(\mathrm{C}_{11}-\mathrm{C}_{22}\right)^2+\left(\mathrm{C}_{13}+\mathrm{C}_{23}\right)^2\\
I_4 &= \frac{1}{8}\left[\mathrm{C}_{11}+\mathrm{C}_{22}-2\left(\mathrm{C}_{12}+\mathrm{C}_{33}\right)\right]^2+\left(\mathrm{C}_{13}-\mathrm{C}_{23}\right)^2\\
I_5 &= \frac{\sqrt{2}}{8}\Big\{8\left(\mathrm{C}_{13}^2-\mathrm{C}_{23}^2\right)\left(\mathrm{C}_{11}-\mathrm{C}_{22}\right)\\
&\qquad +\left[\mathrm{C}_{11}+\mathrm{C}_{22}-2\left(\mathrm{C}_{12}+\mathrm{C}_{33}\right)\right]\left[\left(\mathrm{C}_{11}-\mathrm{C}_{22}\right)^2-2\left(\mathrm{C}_{13}+\mathrm{C}_{23}\right)^2\right]\Big\}
\end{aligned}
$$

$$
\begin{array}{l}
Z_2\\
\quad\Big\downarrow\ I_5^2-I_3^2I_4=0\\
D_2\\
\quad\Big\downarrow\ I_3=0\\
D_4\\
\quad\Big\downarrow\ I_4=0\\
O(2)
\end{array}
$$

Figure 4: Invariant polynomials of planar elasticity tensor (left) and simplified tree of symmetry jumps in 2D (right), François, Chen and Coret (2017)

Our objective is to leverage the classification of 2D microstructures, according to material symmetries, to implement a topology optimization method, aiming to showcase optimal microstructures within each class. This aspect represents a novel investigation within this contribution. The topology optimization method will be succinctly presented in the following section.

3. Double scale topology optimization in the context of linear anisotropic elasticity

Optimizing the design of mechanical systems, and in particular structures, is a topic that has long been the subject of development, particularly in mathematics and mechanics. Among the methods that allow for effective computation of optimized shapes of a mechanical structure, the first was the classical shape optimization method, based on the shape derivative concept (see, e.g., Pironneau, 1984; Sokolowski and Zolésio, 1992). Developments in structural optimization also took off in the second half of the 1980s and into the 1990s, thanks to the progress made in the development of associated mathematical and mechanical theories (see, e.g., Bendsoe, 1984), leading, in particular, to the emergence of the homogenization-based method (see, e.g., Allaire, 2002). This method also led to the development of efficient computational methods, widely appreciated by the engineering community, namely penalty methods, such as SIMP. Finally, a new method emerged in the 1990s, on which we base our study: the method based on the topological derivative. This concept appears as early as the introduction of the bubble-method in Eschenauer, Kobelev and Schumacher (1994). Then, the

rigorous notion of topological derivative was introduced in Sokolowski and Zochowski (1999), which led to numerous developments and advances in the early 2000s (see Novotny and Sokolowski, 2012, for a review), which have continued to expand right up to now, so as to deal with increasingly complex modeling problems (see also Novotny, Sokolowski and Zochowski, 2019; Ferrer and Giusti, 2022). The revival of interest in shape and topology optimization at that time was also due to the improvement of computational techniques, followed by the emergence and democratization of additive manufacturing methods. After pioneering ideas such as in Céa et al. (2000), an impressively efficient new algorithm was introduced in Amstutz and Andrä (2006), based directly on the topological derivative, which led to numerous interesting results, such as, in particular, the optimization of macroscopic Cauchy effect of a 2D periodic material by the design of the underlying unit cell in Giusti et al. (2009), Amstutz et al. (2010). This is precisely the framework we are working in. Let us briefly recall the concept of topological derivative, together with the algorithm from Amstutz and Andrä (2006). We refer to the monographs of Novotny and Sokolowski (2012) and Novotny, Sokolowski and Zochowski (2019) for more details, and to Amstutz et al. (2010) for a presentation in the present framework.

We consider the unit cell of a periodic material $\mathcal{Y}$, which is made of a mixture of a hard material Ω and a soft material $\mathcal{Y} \setminus \overline{\Omega}$. We consider the following optimal shape design problem: find an optimal shape Ω^*, such that $\mathcal{J}(\Omega^*) = \min_{\Omega \subset \mathcal{Y}} \mathcal{J}(\Omega)$, where $\mathcal{J}$ is an objective function. We perturb a given cell $\mathcal{Y}$ in the infinitesimal region, occupied by $B_\rho(\hat{y})$ (see Fig. 5), being filled with different material property than the background. Namely, we introduce either a small ball of soft material into the hard one, or a small ball of hard material into the soft one. Thus, denoting by $\Omega_{\rho,\hat{y}}$ the perturbed distribution of hard material, we define the *topological derivative* of $\mathcal{J}$, written $D_T\mathcal{J}(\Omega)(\hat{y})$ as the first correction term in the following expansion

$$\mathcal{J}(\Omega_{\rho,\hat{y}}) = \mathcal{J}(\Omega) + \rho^2 D_T\mathcal{J}(\Omega)(\hat{y}) + o(\rho^2). \tag{2}$$

The idea of the algorithm, introduced in Amstutz and Andrä (2006), is to use the topological derivative as a necessary local optimality condition for the optimization problem, namely

$$D_T\mathcal{J}(\Omega)(\hat{y}) \geq 0, \forall \hat{y} \in \Omega \cup (\mathcal{Y} \setminus \overline{\Omega}). \tag{3}$$

When describing the distribution by a level-set $\Omega = \{\psi < 0\}$, it can be shown that this optimality condition can be re-written as $\psi = cg_\Omega^T(\psi)$, $c > 0$, where $g_\Omega^T(\psi)$ stands for the *signed topological derivative* associated to $\Omega = \{\psi < 0\}$ (see Novotny, Sokolowski and Zochowski, 2019).

This yields the following algorithm:

- Choose an initial level-set ψ_0
- While $\psi_n \neq g_\Omega^T(\psi_n)$:
  - Update the level-set ψ_{n+1} within a line search making sure that the level-set follows the descent direction: $\mathcal{J}(\Omega_{n+1}) < \mathcal{J}(\Omega_n)$, where $\Omega_{n+1} := \{\psi_{n+1} < 0\}$.
  - Compute $g_\Omega^T(\psi^{n+1})$.

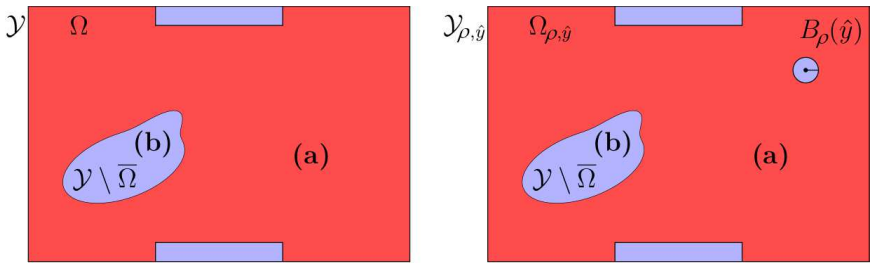

Figure 5: Initial unit cell $\mathcal{Y}$ (left) and perturbed unit cell $\mathcal{Y}_{\rho,\hat{y}}$ (right), Calisti (2021)

4. Numerical results

In this section, we employ the aforementioned optimization algorithm to synthesize microstructures of metamaterial type. Given the significance of auxetics within the realm of metamaterials, our objective is to explore microstructures predisposed to exhibiting a negative Poisson's ratio. This pursuit is underpinned by the acknowledgment that Poisson's ratio is widely regarded in the literature as a pivotal metric for material performance, see Greaves et al. (2011), as it intricately influences the bulk-to-shear modulus ratio, particularly in isotropic and orthotropic materials, as will be discussed further. Subsequently, we will delve into optimizing microstructures for the bulk-to-shear modulus ratio and conduct sensitivity analyses concerning overall porosity, an imperative parameter in the context of weight and energy consumption reduction.

It is worth noting that computations using Voigt's notation (Voigt, 1910) are prone to errors, as demonstrated in the study by Tomáš Mánik (2021). In our study, we adopt the definition provided by Mehrabadi and Cowin (Mehrabadi and Cowin, 1990; Cowin and Mehrabadi, 1992) for the vector representation of strain and stress tensors. This approach incorporates a correction factor of $\sqrt{2}$ for the shear strain and stress components, enabling us to express the two-dimensional homogenized elasticity and compliance tensor in the matrix form

as follows:

$$\underset{\approx}{\mathbf{C}}^{\text{hom}} = \begin{bmatrix} \mathrm{C}^{\text{hom}}_{1111} & \mathrm{C}^{\text{hom}}_{1122} & \sqrt{2}\mathrm{C}^{\text{hom}}_{1112} \\ \mathrm{C}^{\text{hom}}_{1122} & \mathrm{C}^{\text{hom}}_{2222} & \sqrt{2}\mathrm{C}^{\text{hom}}_{2212} \\ \sqrt{2}\mathrm{C}^{\text{hom}}_{1112} & \sqrt{2}\mathrm{C}^{\text{hom}}_{2212} & 2\mathrm{C}^{\text{hom}}_{1212} \end{bmatrix} = \begin{bmatrix} \mathrm{C}_{11} & \mathrm{C}_{12} & \mathrm{C}_{13} \\ \mathrm{C}_{12} & \mathrm{C}_{22} & \mathrm{C}_{23} \\ \mathrm{C}_{13} & \mathrm{C}_{23} & \mathrm{C}_{33} \end{bmatrix}$$

$$\underset{\approx}{\mathbf{S}}^{\text{hom}} = \begin{bmatrix} \mathrm{S}^{\text{hom}}_{1111} & \mathrm{S}^{\text{hom}}_{1122} & \sqrt{2}\mathrm{S}^{\text{hom}}_{1112} \\ \mathrm{S}^{\text{hom}}_{1122} & \mathrm{S}^{\text{hom}}_{2222} & \sqrt{2}\mathrm{S}^{\text{hom}}_{2212} \\ \sqrt{2}\mathrm{S}^{\text{hom}}_{1112} & \sqrt{2}\mathrm{S}^{\text{hom}}_{2212} & 2\mathrm{S}^{\text{hom}}_{1212} \end{bmatrix} = \begin{bmatrix} \mathrm{S}_{11} & \mathrm{S}_{12} & \mathrm{S}_{13} \\ \mathrm{S}_{12} & \mathrm{S}_{22} & \mathrm{S}_{23} \\ \mathrm{S}_{13} & \mathrm{S}_{23} & \mathrm{S}_{33} \end{bmatrix} = \left(\underset{\approx}{\mathbf{C}}^{\text{hom}}\right)^{-1} \tag{4}$$

According to its definition, a continuum with microstructure is characterized by the presence of at least two length scales, which we refer to here and subsequently as macroscopic and microscopic scales, denoted as $\underline{\mathbf{x}}$ and $\underline{\mathbf{y}}$, respectively (see Fig. 6). At the micro scale, the behavior of the material is governed by the following boundary value problem (BVP), posed over the repetitive unit cell $\mathcal{Y}$, obeying a linear elastic Hooke's law type

$$\begin{aligned} \operatorname{div}_y \underset{\sim}{\boldsymbol{\sigma}} &= \underline{\mathbf{0}} \\ \underset{\sim}{\boldsymbol{\sigma}} &= \underset{\approx}{\mathbf{C}}_{\mu} : \underset{\sim}{\boldsymbol{\varepsilon}} \\ \underset{\sim}{\boldsymbol{\varepsilon}} &= \operatorname{grad}^s_y \underline{\mathbf{u}} \\ \underline{\mathbf{u}}\left(\underline{\boldsymbol{\xi}}, \underline{\mathbf{x}}\right) &= \underset{\sim}{\mathbf{E}}\left(\underline{\mathbf{x}}\right) \cdot \underline{\boldsymbol{\xi}} + \underline{\tilde{\mathbf{u}}}\left(\underline{\boldsymbol{\xi}}, \underline{\mathbf{x}}\right) \\ \left\langle \underline{\tilde{\mathbf{u}}} \right\rangle_{\mathcal{Y}} &= 0 \end{aligned} \tag{5}$$

in which $\underset{\sim}{\mathbf{E}}\left(\underline{\mathbf{x}}\right)$ stands for the imposed macrostrain tensor, $\underline{\tilde{\mathbf{u}}}\left(\underline{\boldsymbol{\xi}}, \underline{\mathbf{x}}\right)$ represents the periodic displacement fluctuation and $\underline{\boldsymbol{\xi}}$ is the relative position denoted as

$$\underline{\boldsymbol{\xi}} = \underline{\mathbf{y}} - \underline{\mathbf{x}} \quad \text{such that} \quad \frac{1}{|\mathcal{Y}|}\int_{\mathcal{Y}} \underline{\boldsymbol{\xi}} \, \mathrm{d}V_{\mathcal{Y}} = \underline{\mathbf{0}}. \tag{6}$$

The volume average herein is defined for any field $\psi(\underline{\mathbf{y}})$ as the following integral

$$\langle \psi \rangle_{\mathcal{Y}} = \frac{1}{|\mathcal{Y}|}\int_{\mathcal{Y}} \psi \, \mathrm{d}V_{\mathcal{Y}},$$

with $\mathrm{d}V_{\mathcal{Y}}$ being the infinitesimal integration volume over the unit cell.

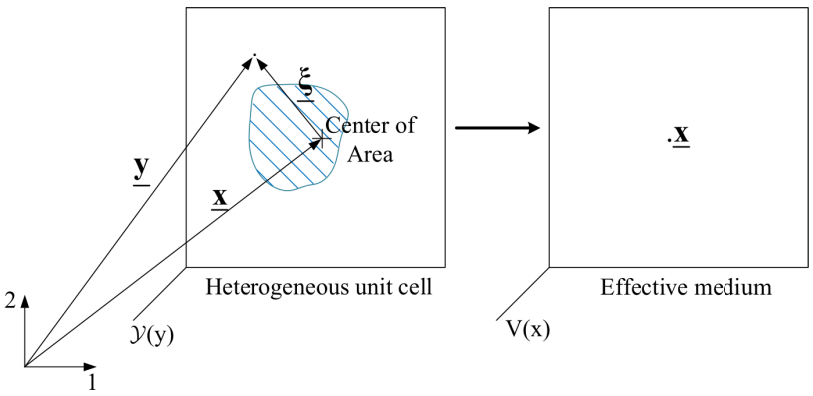

Figure 6: Unit cell of the composite (left) and the effective medium (right), Ganghoffer and Reda (2021)

Insertion of $(5)_2$, $(5)_3$ and $(5)_4$ into $(5)_1$ gives

$$\mathrm{div}_y\left(\underset{\approx}{\mathbf{C}}_\mu : \underset{\approx}{\mathbf{E}}\right) + \mathrm{div}_y\left(\underset{\approx}{\mathbf{C}}_\mu : \mathrm{grad}_y^s \underline{\tilde{\mathbf{u}}}\right) = \underline{\mathbf{0}} \tag{7}$$

which implies, due to the linearity of the PDE of equation (7) with respect to the macroscopic kinematic loading $\underset{\approx}{\mathbf{E}}\left(\underline{\mathbf{x}}\right)$, the existence of a displacement localization tensor, $\underset{\approx}{\mathbf{H}}^{\mathrm{E}}(\underline{\boldsymbol{\xi}})$, such that:

$$\underline{\tilde{\mathbf{u}}}\left(\underline{\boldsymbol{\xi}}, \underline{\mathbf{x}}\right) = \underset{\approx}{\mathbf{H}}^{\mathrm{E}}(\underline{\boldsymbol{\xi}}) : \underset{\approx}{\mathbf{E}}(\underline{\mathbf{x}}). \tag{8}$$

Applying Whitaker's theorem (Whitaker, 1985, 2013) to $(5)_1$ under conditions of continuity of displacement and traction along the internal interfaces between the constituents, we obtain:

$$\langle \mathrm{div}_y \underset{\approx}{\boldsymbol{\sigma}} \rangle_{\mathcal{Y}} = \underline{\mathbf{0}} \Longleftrightarrow \mathrm{div}_x \langle \underset{\approx}{\boldsymbol{\sigma}} \rangle_{\mathcal{Y}} = \underline{\mathbf{0}} \tag{9}$$

where

$$\begin{aligned} \underbrace{\langle \underset{\approx}{\boldsymbol{\sigma}} \rangle_{\mathcal{Y}}}_{\underset{\approx}{\boldsymbol{\Sigma}}} &= \left\langle \underset{\approx}{\mathbf{C}}_\mu : \left(\underset{\approx}{\mathbf{I}} + \mathrm{grad}_y^s \underset{\approx}{\mathbf{H}}^{\mathrm{E}}\right) : \underset{\approx}{\mathbf{E}} \right\rangle_{\mathcal{Y}} \\ &= \underbrace{\left\langle \left(\underset{\approx}{\mathbf{I}} + \mathrm{grad}_y^s \underset{\approx}{\mathbf{H}}^{\mathrm{E}}\right)^{\mathrm{T}} : \underset{\approx}{\mathbf{C}}_\mu : \left(\underset{\approx}{\mathbf{I}} + \mathrm{grad}_y^s \underset{\approx}{\mathbf{H}}^{\mathrm{E}}\right) \right\rangle_{\mathcal{Y}}}_{\underset{\approx}{\mathbf{C}}^{\mathrm{hom}}} : \underset{\approx}{\mathbf{E}}. \end{aligned} \tag{10}$$

By identification, we immediately get the homogenized constitutive law:

$$\underset{\sim}{\boldsymbol{\Sigma}} = \underset{\approx}{\mathbf{C}}^{\mathrm{hom}} : \underset{\sim}{\mathbf{E}} \tag{11}$$

with $\underset{\sim}{\boldsymbol{\Sigma}}$ the macro stress tensor

Letting $\underset{\approx}{\mathbf{A}}^{\mathrm{E}}$ be the strain localization tensor, elaborated as

$$\underset{\approx}{\mathbf{A}}^{\mathrm{E}} = \underset{\approx}{\mathbf{I}} + \mathrm{grad}_y^s \underset{\sim}{\mathbf{H}}^{\mathrm{E}} \tag{12}$$

and combining equations (11) and (12) allow us to deduce the homogenized elasticity tensor as

$$\underset{\approx}{\mathbf{C}}^{\mathrm{hom}} = \left\langle \underset{\approx}{\mathbf{A}}^{\mathrm{E,T}} : \underset{\approx}{\mathbf{C}}_{\mu} : \underset{\approx}{\mathbf{A}}^{\mathrm{E}} \right\rangle_{\mathcal{Y}}. \tag{13}$$

Components of the homogenized compliance tensor can then be computed from those of the homogenized elasticity tensor through the following expressions:

$$\begin{aligned}
\mathrm{S}_{11} &= \frac{\mathrm{C}_{22}\mathrm{C}_{33} - \mathrm{C}_{23}^2}{\left|\underset{\approx}{\mathbf{C}}^{\mathrm{hom}}\right|} \\
\mathrm{S}_{22} &= \frac{\mathrm{C}_{11}\mathrm{C}_{33} - \mathrm{C}_{13}^2}{\left|\underset{\approx}{\mathbf{C}}^{\mathrm{hom}}\right|} \\
\mathrm{S}_{33} &= \frac{\mathrm{C}_{11}\mathrm{C}_{22} - \mathrm{C}_{12}^2}{\left|\underset{\approx}{\mathbf{C}}^{\mathrm{hom}}\right|} \\
\mathrm{S}_{23} &= -\frac{\mathrm{C}_{11}\mathrm{C}_{23} - \mathrm{C}_{12}\mathrm{C}_{13}}{\left|\underset{\approx}{\mathbf{C}}^{\mathrm{hom}}\right|} \\
\mathrm{S}_{13} &= -\frac{\mathrm{C}_{22}\mathrm{C}_{13} - \mathrm{C}_{12}\mathrm{C}_{23}}{\left|\underset{\approx}{\mathbf{C}}^{\mathrm{hom}}\right|} \\
\mathrm{S}_{12} &= -\frac{\mathrm{C}_{33}\mathrm{C}_{12} - \mathrm{C}_{13}\mathrm{C}_{23}}{\left|\underset{\approx}{\mathbf{C}}^{\mathrm{hom}}\right|}
\end{aligned} \tag{14}$$

with $\left|\underset{\approx}{\mathbf{C}}^{\mathrm{hom}}\right|$ being the determinant of elasticity tensor $\underset{\approx}{\mathbf{C}}^{\mathrm{hom}}$, expressed as

$$\left|\underset{\approx}{\mathbf{C}}^{\mathrm{hom}}\right| = \mathrm{C}_{11}\mathrm{C}_{22}\mathrm{C}_{33} + 2\mathrm{C}_{12}\mathrm{C}_{13}\mathrm{C}_{23} - \mathrm{C}_{11}\mathrm{C}_{23}^2 - \mathrm{C}_{22}\mathrm{C}_{13}^2 - \mathrm{C}_{33}\mathrm{C}_{12}^2. \tag{15}$$

All numerical simulations consider topology optimization problems, having the general form:

$$\inf_{\Omega\in\mathcal{U}_{\mathrm{ad}}} \mathcal{J}(\Omega) := j\left(\underset{\approx}{\mathbf{C}}_{\Omega}^{\mathrm{hom}}\right) \tag{16}$$

where Ω is a subdomain of the unit cell, a unit square, $\mathcal{Y} := (0,1)\times(0,1)$. The sequence of domains $(\Omega_n)_{n\geqslant 0}$, produced by the optimization process, are defined by the elaboration of a level set function, viz.; $\Omega_n = \{\psi_n < 0\}$ and $\mathcal{Y}\backslash\overline{\Omega_n} = \{\psi_n > 0\}$, the hard and soft phases, respectively, where ψ_n is the level-set at a given step n of the descent towards the optimum.

Both soft and hard phase domains are characterized by the same Poisson's ratio ($\nu = 0.3$), but by two distinct Young's moduli, respectively, $E_{\{\psi<0\}} = 1$ (material 1), $E_{\{\psi>0\}} = 0.001$ (material 2). That is, we consider a phase contrast parameter $\gamma_0 = 0.001$. The topology optimization is in fact exchanging the soft and hard phases, with a non nil contrast parameter to avoid singular perturbations of the topology corresponding to a true void. The initial distribution of material $\Gamma_0 = \{x \in \mathcal{Y} \mid \psi_0(x) = 0\}$ is a disk, given by the initial level-set function ψ_0, defined by

$$\psi_0(x,y) = \cos\left[\pi(x-0.5)\right]^2 \cos\left[\pi(y-0.5)\right]^2 - 0.5. \tag{17}$$

The topology of the unit cell for this case is depicted in Fig. 7, where the black- and white-coloured areas denote, respectively, materials 1 (the hard phase) and 2 (the soft phase). Also illustrated in Fig. 7 is the initial finite element mesh, exploited for numerical simulations. It consists of a number of squares $n_i = 40$ along one side of the unit cell $\mathcal{Y}$, with four triangles per square, resulting in 6400 linear triangular elements in total.

4.1. Topology optimization of Poisson's ratio

An optimal Poisson's ratio of periodic microstructures is searched in this section using the topology optimization method exposed in Section 3 in the different symmetry classes of Table 1. Namely, we will consider the minimization of Poisson's ratio with the following general functionals including a penalization to enforce the considered material symmetry:

$$\begin{aligned}
j(\nu_{12}) &= \frac{\mathrm{C}_{12}}{\mathrm{C}_{22}} + \beta\cdot(\mathrm{I}_5^2 - \mathrm{I}_3^2\mathrm{I}_4) && \text{for orthotropic material}\\
j(\nu_{12}) &= \frac{\mathrm{C}_{12}}{\mathrm{C}_{22}} + \beta\cdot(\mathrm{I}_3) && \text{for tetragonal material}\\
j(\nu_{12}) &= \frac{\mathrm{C}_{12}}{\mathrm{C}_{22}} + \beta_1\cdot(\mathrm{I}_3) + \beta_2\cdot(\mathrm{I}_4) && \text{for isotropic material.}
\end{aligned} \tag{18}$$

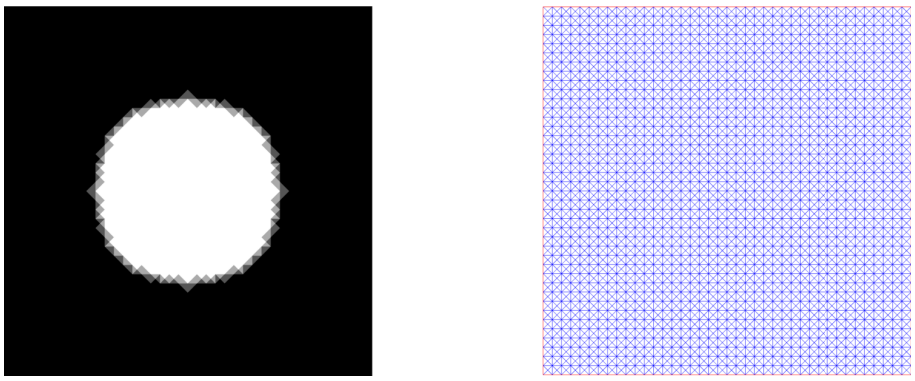

Figure 7: Initial distribution of material for the optimum topology (left) and initial adopted finite element mesh (right)

The following figures show one optimal microstructure for each of the three symmetry classes (successively orthotropic, tetragonal and isotropic), both at the scale of a single unit cell, and repeated within a macroscopic domain for the sake of clarity of the presentation of results.

4.1.1. Orthotropic case

In this first example, the objective is to minimize Poisson's ratio for orthotropic materials using the functional in expression $(18)_1$. The imposed vanishing invariant for this class of materials (D_2) is $I_5^2 - I_3^2 I_4 = 0$, as illustrated in Fig. 8(a). The final material distribution, corresponding to the optimized level-set, reached after 63 iterations, is depicted in Fig. 8(b). The resulting periodically repeated optimal microstructure is shown in Fig. 8(c). At the end of the optimization, the volume fraction is 53.1221%. It is important to note that there is no constraint on the volume fraction. The resulting small value of the penalized invariant is $\mathrm{I}_5^2 - \mathrm{I}_3^2 \mathrm{I}_4 \simeq 0.0003$, indicating the effectiveness of the penalization method.

Figure 9 illustrates the convergence history, displaying the angle θ, plotted against the number of iterations. Three instances of local mesh refinement are observed: at iteration 29, where the angle is approximately $\theta \simeq 91.921°$; again at iteration 32 with the angle around $\theta \simeq 91.5598°$; and finally, at iteration 52, where the angle θ reaches an approximate value of $14.494°$. The total number of iterations, required to achieve the final distribution, with an angle of approximately $\theta \simeq 9.1865°$, is 63.

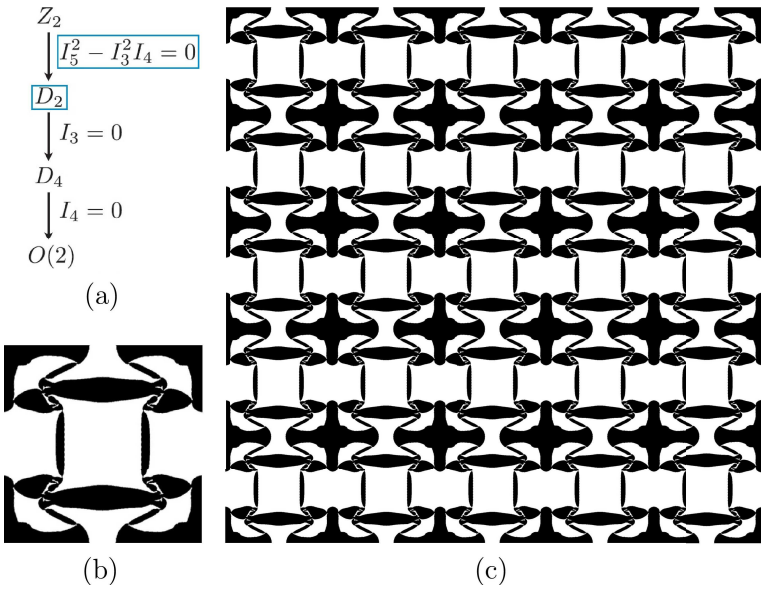

Figure 8: Minimization of Poisson's ratio, $\nu_{12} = \frac{C_{12}}{C_{22}}$: (a) imposed invariant, (b) optimal unit cell, and (c) corresponding periodic optimal microstructure

The corresponding value of homogenized elasticity tensor is given by

$$\underset{\approx}{\mathbf{C}}^{\text{hom}} = \begin{bmatrix} 0.11616 & -0.021125 & 0 \\ -0.021125 & 0.0085737 & 0 \\ 0 & 0 & 0.0010784 \end{bmatrix} \text{(MPa)} \tag{19}$$

which yields a negative Poisson's ratio, $\nu_{12} = -2.464$.

4.1.2. Tetragonal case

The sufficient condition for membership in D_4, corresponding to tetragonal materials, is $I_3 = 0$, as illustrated in Fig. 10(a). To satisfy this condition, the functional for minimizing Poisson's ratio is expressed as $(18)_2$. The final optimized unit cell topology, attained in 41 iterations, and the corresponding periodic optimal microstructure are successively shown in Figs. 10(b) and 10(c). The final volume fraction in this case is 55.0008%. The small value of the penalized invariant, $\mathrm{I}_3 \simeq 5.5714 \times 10^{-5}$, also demonstrates the efficiency of the penalization

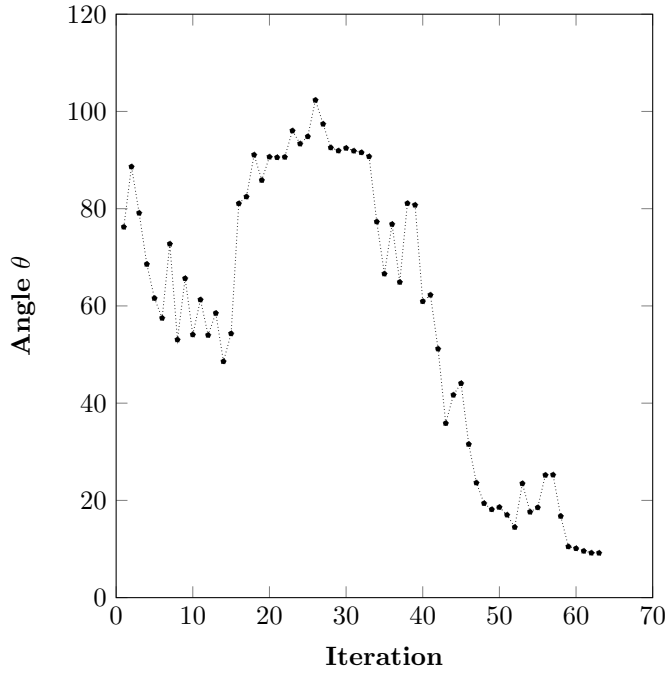

Figure 9: Convergence history: angle θ with respect to the number of iterations

method. It is worth noting that the resulting topology is more symmetrical compared to the one obtained for the orthotropic case.

The associated effective homogenized moduli tensor is computed as the following matrix with numerical entries

$$\underset{\approx}{\mathbf{C}}^{\text{hom}} = \begin{bmatrix} 0.0106 & -0.022991 & 0 \\ -0.022991 & 0.0106 & 0 \\ 0 & 0 & 0.0017685 \end{bmatrix} \text{(MPa)} \tag{20}$$

which results in a negative Poisson's ratio, $\nu_{12} = -2.1689$.

4.1.3. Isotropic case

In order for a material to be a member of the isotropic group $O(2)$, both $I_3 = 0$ and $I_4 = 0$ must hold, as exhibited in Fig. 11(a). For this case, we utilize the functional $(18)_3$ to minimize Poisson's ratio. After completing the optimization, the volume fraction reaches 77.7883%. The converged optimum unit cell,

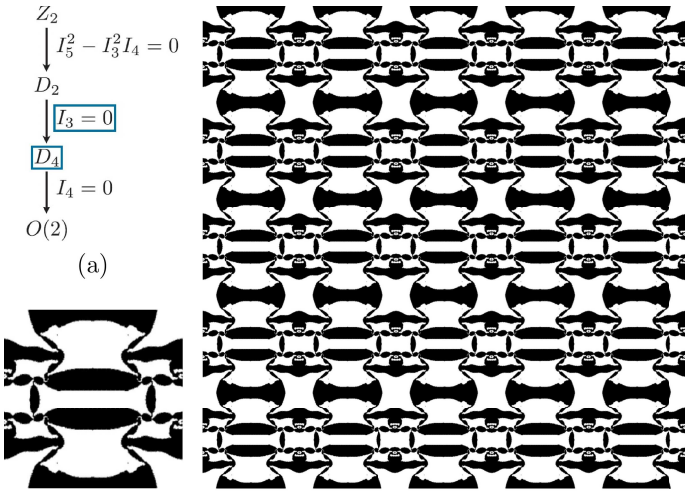

Figure 10: Minimization of Poisson's ratio, $\nu_{12} = \frac{C_{12}}{C_{22}}$: (a) imposed invariant, (b) optimum unit cell, and (c) corresponding periodic optimal microstructure

achieved in 29 iterations, is presented in Fig. 11(b), while the corresponding periodic microstructure is shown in Fig. 11(c). However, despite the very small values of the two penalized invariants ($I_3 \simeq 9.7429 \times 10^{-5}$, $I_4 \simeq 0.00103$), it appears that the microstructure does not satisfy the imposed isotropy constraint. The hexachiral lattice stands as one well-known example of an auxetic isotropic material, which may, however, necessitate the consideration of chirality through an enhanced constitutive law of strain gradient type (see Calisti et al., 2023).

The homogenized elasticity tensor is expressed as the following 3x3 matrix with numerical values given by

$$\underset{\approx}{\mathbf{C}}^{\text{hom}} = \begin{bmatrix} 0.039472 & -0.019467 & 0 \\ -0.019467 & 0.025512 & 0 \\ 0 & 0 & 0.0032902 \end{bmatrix} \text{(MPa)} \tag{21}$$

and the resulting negative Poisson's ratio, $\nu_{12} = -0.76305$.

It can be seen that the three synthesized microstructures exhibit a re-entrant type mechanism, a well-known characteristic of auxetics (see also Ganghoffer et al., 2018). Note that the rolling mechanisms for chiral microstructures apparently require a higher order effective model.

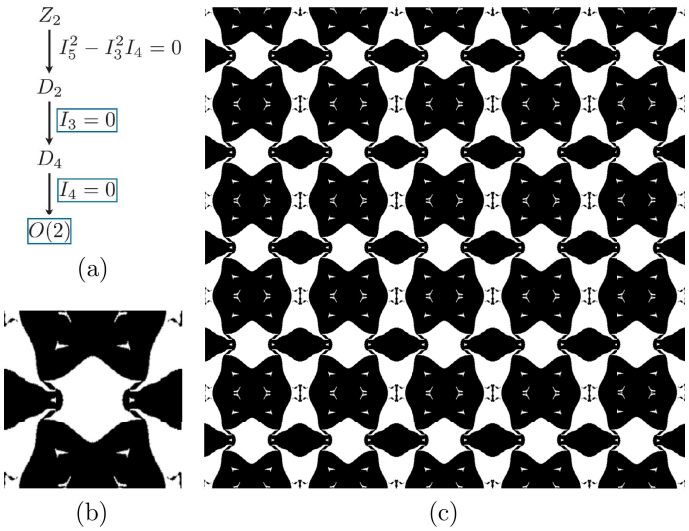

Figure 11: Minimization of Poisson's ratio, $\nu_{12} = \frac{C_{12}}{C_{22}}$: (a) imposed invariant, (b) optimum unit cell, and (c) corresponding periodic structure

In the next section, the aim is to synthesize microstructures with an optimal bulk-to-shear modulus ratio, which serves as an indicator of a potential metamaterial behavior.

4.2. Topology optimization of the ratio of bulk to shear modulus

4.2.1. Formulation

In an orthotropic medium, the two-dimensional compliance tensor has the following structure:

$$\underset{\approx}{\mathbf{S}} = \begin{bmatrix} \frac{1}{E_1} & -\frac{\nu_{12}}{E_1} & 0 \\ -\frac{\nu_{12}}{E_1} & \frac{1}{E_2} & 0 \\ 0 & 0 & \frac{1}{2\mu_{12}} \end{bmatrix} \tag{22}$$

where E_1 and E_2 are the Young's moduli in the x and y directions, respectively, and ν_{12} is the Poisson's ratio between the x and y directions. The shear modulus,

μ_{12}, is given by:

$$\mu_{12} = \frac{\mathrm{E}_1\mathrm{E}_2}{\mathrm{E}_1 + \mathrm{E}_2 + 2\mathrm{E}_2\nu_{12}} = \mathrm{G}. \tag{23}$$

Utilizing the expression in Equation $(1)_4$, we can express the bulk modulus in two dimensions is expressed as:

$$\mathrm{K}^{2\mathrm{D}} = \frac{1}{\mathrm{S}_{11} + \mathrm{S}_{22} + 2\mathrm{S}_{12}} = \frac{\mathrm{E}_1\mathrm{E}_2}{\mathrm{E}_1 + \mathrm{E}_2\left(1 - 2\nu_{12}\right)}. \tag{24}$$

To ensure the fulfilment of positivity condition $\mathrm{K}^{2\mathrm{D}} > 0$, the denominator of expression (24) must be positive, providing an upper bound for Poisson's ratio:

$$\mathrm{E}_1 + \mathrm{E}_2\left(1 - 2\nu_{12}\right) > 0 \Longrightarrow \nu_{12} < \frac{1 + \frac{\mathrm{E}_1}{\mathrm{E}_2}}{2}. \tag{25}$$

Additionally, the condition $\frac{\mathrm{K}^{2\mathrm{D}}}{\mathrm{G}} > 0$ yields a lower bound for Poisson's ratio:

$$\frac{\mathrm{E}_1 + \mathrm{E}_2 + 2\mathrm{E}_2\nu_{12}}{\mathrm{E}_1 + \mathrm{E}_2\left(1 - 2\nu_{12}\right)} > 0 \Longrightarrow \nu_{12} > -\frac{1 + \frac{\mathrm{E}_1}{\mathrm{E}_2}}{2}. \tag{26}$$

Upon combining the upper and lower bounds, the following bounds for Poisson's ratio are obtained in the 2D situation:

$$-\frac{1 + \frac{\mathrm{E}_1}{\mathrm{E}_2}}{2} < \nu_{12} < \frac{1 + \frac{\mathrm{E}_1}{\mathrm{E}_2}}{2}. \tag{27}$$

In contrast to the 3D case, we observe the lack of fixed bounds for Poisson's ratio in general for the 2D situation, as the ratio of effective moduli can vary widely. Anisotropy plays a crucial role in expanding these bounds, particularly for auxetic materials, requiring pronounced anisotropy to achieve more negative Poisson's ratio values.

For an isotropic or tetragonal material with $\mathrm{E}_1 = \mathrm{E}_2 = \mathrm{E}$ and $\nu_{12} = \nu_{21} = \nu$, the expressions for the bulk and shear moduli, the ratio of bulk to shear modulus, and the bounds of Poisson's ratio are given, respectively, as follows:

$$
\begin{aligned}
\mathrm{K}^{\mathrm{2D}} &= \frac{\mathrm{E}}{2(1-\nu)} \\
\mathrm{G} &= \frac{\mathrm{E}}{2(1+\nu)} \\
\frac{\mathrm{K}^{\mathrm{2D}}}{\mathrm{G}} &= \frac{1+\nu}{1-\nu} \\
-1 < \nu < 1.
\end{aligned}
\tag{28}
$$

We note that in the 2D situation, Poisson's ratio can reach values as high as unity, contrary to the 3D case, where it is limited to $\frac{1}{2}$. In Fig. 12, we plot the bulk-to-shear modulus ratio versus Poisson's ratio for different ratios of the two tensile moduli. Increasing the ratio of tensile moduli results in a more pronounced auxetic effect, confirming the previously established general statement, regarding the obtained bounds.

It is important to stress that topology optimization delivers only locally optimal microstructures, so the obtained optima are expected to strongly depend on both the initial topology and the set of material parameters, inherent to the algorithm.

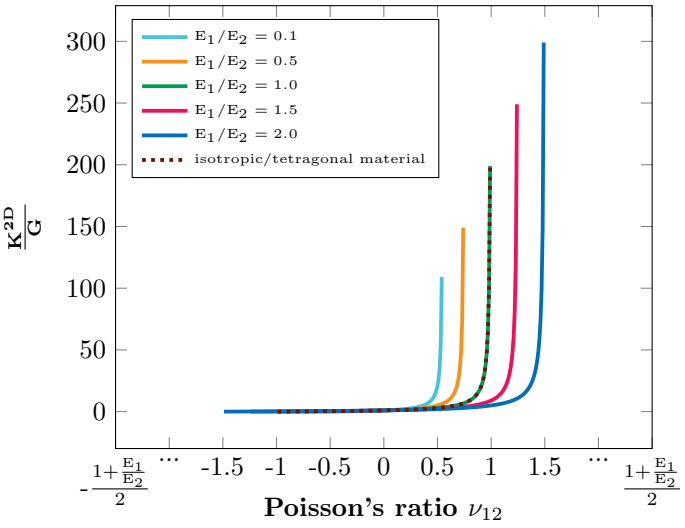

Figure 12: $\frac{\mathrm{K}^{\mathrm{2D}}}{\mathrm{G}}$ versus Poisson's ratio diagram in 2D for orthotropic, tetragonal and isotropic materials

4.2.2. Minimization of the ratio of bulk to shear modulus

With the above results at hand, we now carry out the minimization of the ratio of bulk to shear modulus. It is important to note herein that in order to get the simplified symmetry in 2D for orthotropic, tetragonal and isotropic material (see also Fig. 4) we impose the corresponding jump conditions, based on the polynomial invariants of the homogenized elasticity tensor, by adding penalization terms within the functional to be optimized. Additionally, in order to even more constraint the search for negative Poisson's ratio, we add the penalization term $\left(\frac{\mathrm{C}_{12}}{\mathrm{C}_{22}}+1\right)^2$, representing the target value of -1 for Poisson's ratio. Finally, the cost functions for the orthotropic, tetragonal and isotropic material symmetries take, successively, the forms

$$
\begin{aligned}
j\left(\frac{\mathrm{K}^{\mathrm{2D}}}{\mathrm{G}}\right) &= \frac{2\mathrm{S}_{33}}{\mathrm{S}_{11}+\mathrm{S}_{22}+2\mathrm{S}_{12}} + \beta_1 \cdot \left(\frac{\mathrm{C}_{12}}{\mathrm{C}_{22}}+1\right)^2 + \beta_2 \cdot (\mathrm{I}_5^2 - \mathrm{I}_3^2\mathrm{I}_4) \\
j\left(\frac{\mathrm{K}^{\mathrm{2D}}}{\mathrm{G}}\right) &= \frac{2\mathrm{S}_{33}}{\mathrm{S}_{11}+\mathrm{S}_{22}+2\mathrm{S}_{12}} + \beta_1 \cdot \left(\frac{\mathrm{C}_{12}}{\mathrm{C}_{22}}+1\right)^2 + \beta_2 \cdot (\mathrm{I}_3) \\
j\left(\frac{\mathrm{K}^{\mathrm{2D}}}{\mathrm{G}}\right) &= \frac{2\mathrm{S}_{33}}{\mathrm{S}_{11}+\mathrm{S}_{22}+2\mathrm{S}_{12}} + \beta_1 \cdot \left(\frac{\mathrm{C}_{12}}{\mathrm{C}_{22}}+1\right)^2 + \beta_2 \cdot (\mathrm{I}_3) + \beta_3 \cdot (\mathrm{I}_4).
\end{aligned}
\tag{29}
$$

4.2.2.1. Orthotropic case

The first scenario of interest involves minimizing the ratio of bulk to shear modulus for orthotropic materials using expression $(29)_1$. The imposed invariant for this case is indicated in Fig. 13(a). The optimized topology of the unit cell and the resulting periodic microstructure are shown in Figs. 13(b) and 13(c), respectively. The total number of iterations, required to achieve convergence is 39 (including iterations for two local refinements of the mesh). The volume fraction at the end of the numerical simulation is 72.5901%.

The matrix representation of the obtained optimal homogenized elasticity tensor is given by

$$
\underset{\approx}{\mathbf{C}}^{\mathrm{hom}} = \begin{bmatrix} 0.013255 & -0.011284 & 0 \\ -0.011284 & 0.060504 & 0 \\ 0 & 0 & 0.029901 \end{bmatrix} (\mathrm{MPa}). \tag{30}
$$

From this, the final values of the ratio of bulk to shear modulus and the

Poisson's ratio can be computed: $\frac{\mathrm{K^{2D}}}{\mathrm{G}} = 0.23423$, $\nu_{12} = -0.1865$. The very small value of the penalized invariant for the present case is $\mathrm{I}_5^2 - \mathrm{I}_3^2\mathrm{I}_4 \simeq 2.5849 \times 10^{-26}$.

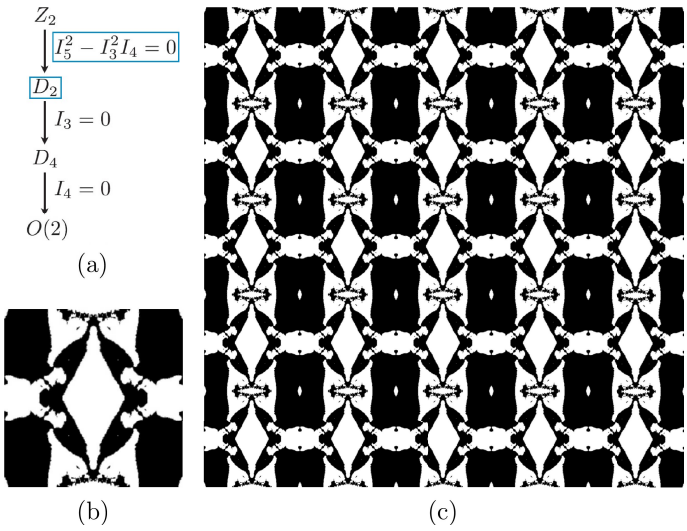

Figure 13: Minimization of the ratio of bulk to shear modulus, $\frac{\mathrm{K^{2D}}}{\mathrm{G}}$, for the orthotropic case: (a) imposed invariant, (b) optimum unit cell, and (c) corresponding optimum periodic structure

4.2.2.2. Tetragonal case

We now turn our attention to the cost function, expressed in $(29)_2$, aimed at minimizing the ratio of bulk to shear modulus for tetragonal materials. The sufficient and necessary condition for satisfying this material symmetry, that is, $I_3 = 0$, is depicted in Fig. 14(a). After 45 iterations, the optimal distribution of materials is illustrated in Fig. 14(b), along with the corresponding periodically repeated microstructure in Fig. 14 (c). In this example, the final volume fraction reaches 63.4823%.

The resulting homogenized elasticity tensor is represented in matrix format as

$$\underset{\approx}{\mathbf{C}}^{\mathrm{hom}} = \begin{bmatrix} 0.02524 & -0.0080492 & 0 \\ -0.0080492 & 0.02524 & 0 \\ 0 & 0 & 0.012329 \end{bmatrix} (\mathrm{MPa}), \tag{31}$$

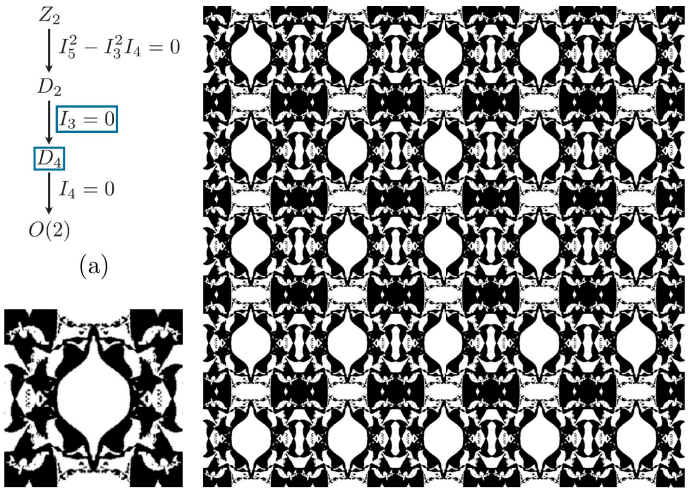

Figure 14: Minimization of the ratio of bulk to shear modulus, $\frac{\mathrm{K^{2D}}}{\mathrm{G}}$, for the tetragonal case: (a) imposed invariant, (b) optimum unit cell, and (c) corresponding optimum periodic structure

which allows us to compute the optimal value of the ratio of bulk to shear modulus, $\frac{\mathrm{K^{2D}}}{\mathrm{G}} = 0.83071$, as well as the resulting negative Poisson's ratio, $\nu_{12} = -0.3189$. The penalized invariant for this case is $\mathrm{I}_3 \simeq 2.6694 \times 10^{-5}$, indicating a small value.

4.2.2.3. Isotropic case

In this example, the primary focus lies in minimizing the ratio of bulk to shear modulus for isotropic materials. The objective function, represented by expression $(29)_3$, serves this purpose. The required invariants, demanding both $I_3 = 0$ and $I_4 = 0$ for this symmetry class, are presented in Fig. 15(a). Illustrations of the optimal unit cell and the corresponding periodic microstructure, achieved after 30 iterations, are presented in Figs. 15(b) and 15(c), respectively. Upon completing the topology optimization, the volume fraction stabilizes at 74.6208%.

The matrix form of the resulting homogenized elasticity tensor is delineated by the values in equation (32). It is imperative to highlight that while the optimal periodic structure bears a striking resemblance to the isotropic class,

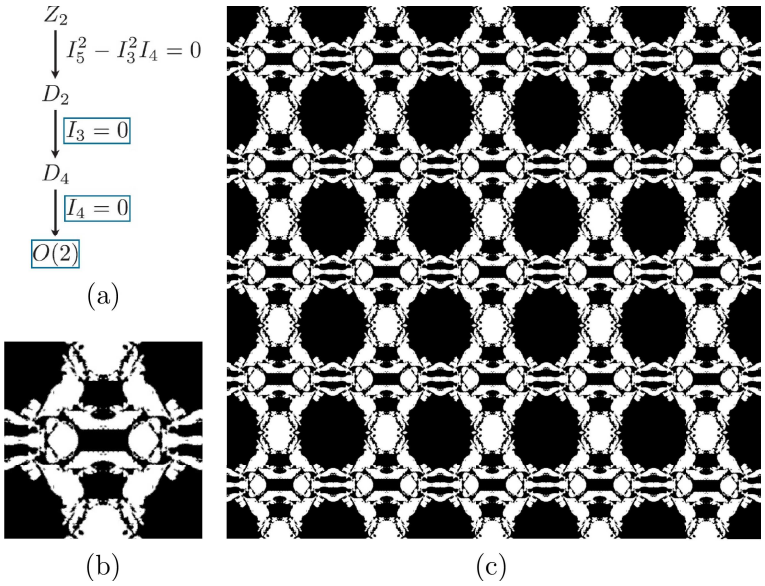

Figure 15: Minimization of the ratio of bulk to shear modulus, $\frac{\mathrm{K^{2D}}}{\mathrm{G}}$, for the isotropic case: (a) imposed invariant, (b) optimum unit cell, and (c) corresponding optimum periodic structure

it does not entirely fulfill the imposed isotropy constraint. Consequently, the count of independent components within the homogenized tensor is not two, as illustrated in Fig. 3,

$$\underset{\approx}{\mathbf{C}}^{\mathrm{hom}} = \begin{bmatrix} 0.02363 & -0.0077573 & 0 \\ -0.0077573 & 0.021773 & 0 \\ 0 & 0 & 0.0094077 \end{bmatrix} \text{(MPa)}, \tag{32}$$

from which we can easily compute the values of the ratio of bulk to shear modulus ($\frac{\mathrm{K^{2D}}}{\mathrm{G}} = 0.79275$) and the negative Poisson's ratio ($\nu_{12} = -0.35629$). The two penalized invariants, which are evaluated as $\mathrm{I}_3 \simeq 1.7257 \times 10^{-6}, \mathrm{I}_4 \simeq 6.7785 \times 10^{-5}$, show very small values.

For enhanced clarity, we have consolidated the optimal unit cells acquired through minimizing the ratio of bulk to shear modulus for orthotropic, tetragonal, and isotropic materials onto the diagram of $\frac{\mathrm{K^{2D}}}{\mathrm{G}}$ versus Poisson's ratio, as depicted in Fig. 16. It is evident that, among the three material types considered

(orthotropic, tetragonal, and isotropic), orthotropic materials most effectively achieve the objective of minimizing the ratio of bulk to shear modulus.

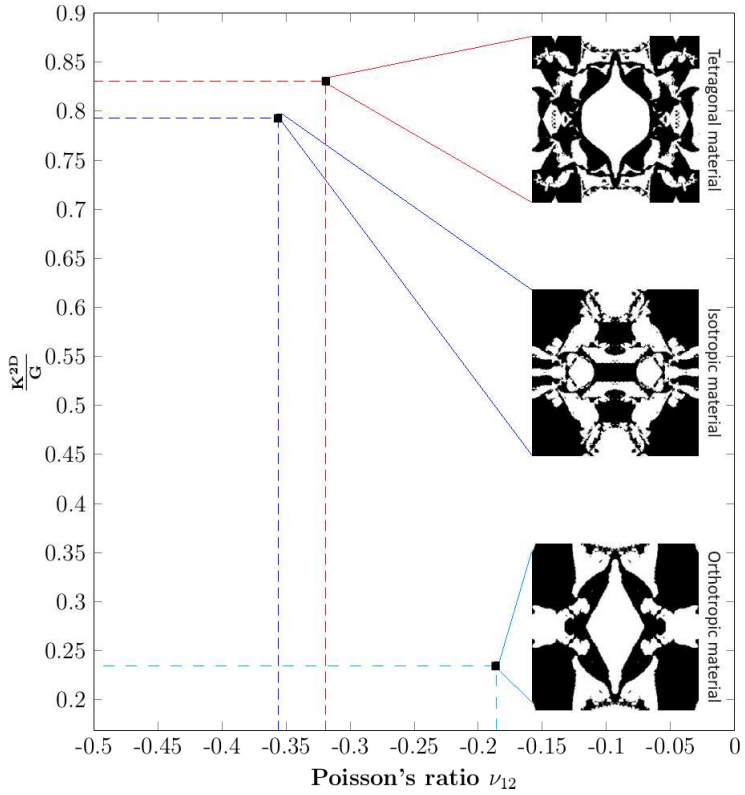

Figure 16: Optimum unit cells obtained after minimization of the ratio of bulk to shear modulus for orthotropic, tetragonal and isotropic materials on the diagram of $\frac{K^{2D}}{G}$ versus Poisson's ratio

We proceed by analyzing the sensitivity of results to changes in the contrast parameter, mesh size, and initial level-set. To this end, we address the minimization problem, defined in $(29)_3$ across several contrast parameter values, namely $\{0.0001, 0.001, 0.01\}$. Additionally, we vary the initial mesh sizes, denoted by n_i, with n_i taking values from the set $\{40, 60, 70\}$. Furthermore, we introduce perturbations to the initial level-set ψ_0, defined in (17), by varying i within the set $\{-4, -2, 2\}$, resulting in modified level-set functions, expressed as:

$$\psi_{0,i} := \psi_0 + i * 0.05. \tag{33}$$

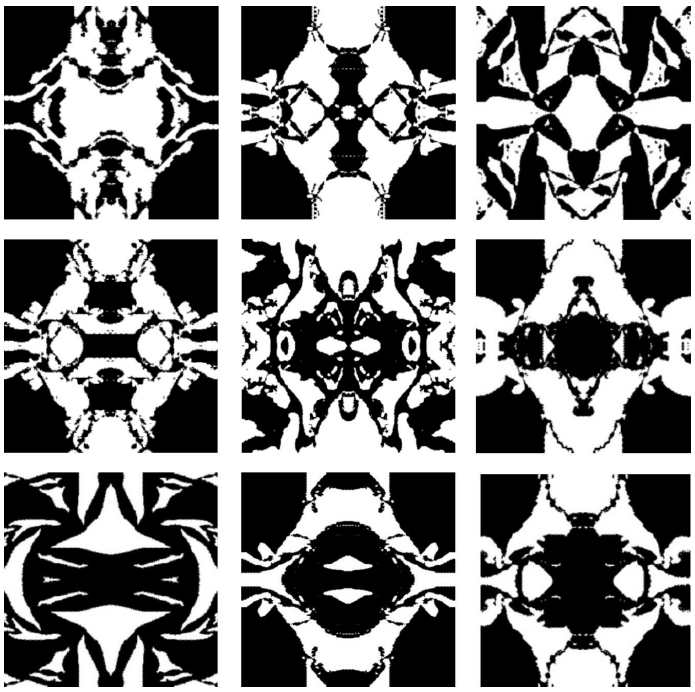

Figure 17: Sensitivity analysis: contrast parameter in the first column in the set (0.0001, 0.001 and 0.01, from top to bottom, respectively), mesh size in second column in the set ($n_i = 40$, $n_i = 60$ and $n_i = 70$, from top to bottom, respectively), and initial level-set in the third column ($i = -4$, $i = -2$ and $i = 2$, from top to bottom, respectively)

All three parameters have a significant impact on the optimal design. It is crucial to emphasize that topology optimization typically yields local minima, indicating that the obtained minima are heavily influenced by the selected initial parameter values.

4.2.3. Maximization of the ratio of bulk to shear modulus

Finally, to end this section, we examine the maximization of the ratio of bulk to shear modulus by minimizing the following functional without enforcing any constraints, as outlined in expression (34),

$$j\left(\frac{\mathrm{K}^{2\mathrm{D}}}{\mathrm{G}}\right) = -\frac{2\mathrm{S}_{33}}{\mathrm{S}_{11}+\mathrm{S}_{22}+2\mathrm{S}_{12}}. \tag{34}$$

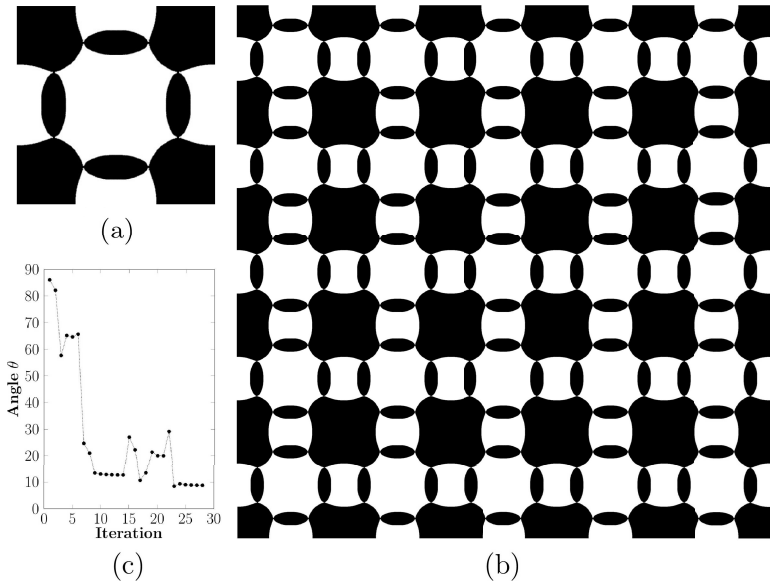

Figure 18: Maximization of the ratio of bulk to shear modulus, $\frac{\mathrm{K^{2D}}}{\mathrm{G}}$: (a) optimum unit cell, (b) corresponding periodic structure, and (c) convergence history of the cost function: angle θ with respect to the number of iterations

The optimized topology, achieved after 28 iterations, is presented in Fig. 18, alongside the corresponding periodic microstructure. The convergence history, tracking the evolution of the angle θ across iterations, is depicted in Fig. 18(c). To attain convergence, with an angle of approximately $\theta \simeq 8.7576°$, we conducted three local mesh refinements: at iteration 5, yielding a residual angle of approximately $\theta \simeq 64.6569°$; at iteration 14, resulting in an angle of approximately $\theta \simeq 12.646°$; and, finally, at iteration 21, where the angle θ reaches approximately $19.9999°$. In this case, the final volume fraction after the topology optimization is 64.3895%.

The associated homogenized elasticity tensor, from which the final value of the ratio of bulk to shear modulus can be computed, $\frac{\mathrm{K^{2D}}}{\mathrm{G}} = 81.3268$, has the following form

$$\underset{\approx}{\mathbf{C}}^{\mathrm{hom}} = \begin{bmatrix} 0.16859 & 0.013008 & 0 \\ 0.013008 & 0.16859 & 0 \\ 0 & 0 & 0.0011165 \end{bmatrix} \text{(MPa)}. \tag{35}$$

Demonstrably, it is an elasticity tensor of a tetragonal material with three independent components (see also Fig. 3).

5. Conclusion

In this paper, we present optimal periodic microstructures for mechanical metamaterials using a methodology based on topology optimization. Specifically, we leverage the topological derivative, introduced in Novotny and Sokolowski (2012), to assess the sensitivity of a functional to changes in the topology within the reference unit cell. Remarkably, the topological derivative is a function that enables the design of a numerical scheme, based on the descent direction of the functional toward a minimum.

We focused on Poisson's ratio and the bulk-to-shear modulus ratio as key performance indicators to categorize different classes of mechanical metamaterials. Auxetics, a type of metamaterial with a large capacity for volumetric change (area change in 2D), exhibit high resistance to shock, impact, vibration, and sound propagation. Similarly, the ratio of bulk to shear moduli can also be considered as a performance index of the resistance to shear versus volumetric changes.

The optimal microstructures we obtained are local minima within three 2D symmetry classes: orthotropic, tetragonal, and isotropic. Transitioning between classes involves applying a penalization approach by zeroing corresponding invariants. The optimization process was efficient, converging in roughly 35 iterations.

Our results demonstrate the sensitivity of the topology optimization method to parameters such as mesh size, initial level-set function, and contrast parameter of moduli. As expected, the outcomes represent local minima. We are currently applying the proposed methodology to other types of multi-scale higher-order effective models. The progress of this work will be documented and reported in forthcoming publications.

Acknowledgements

Xuan-Nam Do and Jean-François Ganghoffer would like to thank DGA (Délégation Générale de l'Armement) for the funding of this work under the research project CORPLAUX.

Valentin Calisti has been funded by Praemium Academiæ of Š. Nečasová, in the Institute of Mathematics, supported by the Czech Academy of Sciences (RVO 67985840). This support is gratefully acknowledged.

References

Allaire, G. (2002) *Shape Optimization by the Homogenization Method*. Springer-Verlag, New York.

Amstutz, S. and Andrä, H. (2006) A new algorithm for topology optimization using a level-set method. *Journal of Computational Physics*, **216**(2) 573–588.

Amstutz, S., Giusti, S.M., Novotny, A.A. and de Souza Neto, E.A. (2010) Topological derivative for multi-scale linear elasticity models applied to the synthesis of microstructures. *International Journal for Numerical Methods in Engineering*, **84**(6) 733–756.

Bacigalupo, A. and Gambarotta, L. (2014) Homogenization of periodic hexa- and tetrachiral cellular solids. *Composite Structures*, **116** 461–476.

Bechterew, P. (1926) Analytical study of the generalized Hooke's law. Application of the method of coordinate transformation. *Zh. Russ. Fiz.-Khim. Obshch. Leningrad. Univ., Fizika*, **58**(3) 415–416.

Bendsøe, M.P. (1984) *Optimal Shape Design for Elliptic Systems*. Springer-Verlag, New York.

Bertoldi, K., Vitelli, V., Christensen, J. and Van Hecke, M. (2017) Flexible mechanical metamaterials. *Nature Reviews Materials*, **2**(11) 1–11.

Calisti, V. (2021) Synthése de microstructures par optimisation topologique, et optimisation de forme d'un problème d'interaction fluide-structure. PhD thesis, Université de Lorraine.

Calisti, V., Lebée, A., Novotny, A.A. and Sokolowski, J. (2023) Emergence of elastostatic strain-gradient effects from topological optimization. *European Journal of Mechanics-A/Solids*, 100 104979.

Céa, J., Garreau, S., Guillaume, P. and Masmoudi, M. (2000) The shape and topological optimizations connection. *Computer Methods in Applied Me-chanics and Engineering*, 188 713–726.

Cowin, S.C. and Mehrabadi, M.M. (1992) The structure of the linear anisotropic elastic symmetries. *Journal of the Mechanics and Physics of Solids*, **40**(7) 1459–1471.

De Saxcé, G. and Vallée, C. (2013) Invariant measures of the lack of symmetry with respect to the symmetry groups of 2D elasticity tensors. *Journal of Elasticity*, **111**(1) 21–39.

Eschenauer, H.A., Kobelev, V. and Schumacher, A. (1994) Bubble method for topology and shape optimization of structures. *Structural and Multi-disciplinary Optimization*, 8 42–51.

Ferrer, A. and Giusti, S.M. (2022) Inverse homogenization using the topological derivative. *Engineering Computations*, **39**(1) 337–353.

François, M.L.M., Chen, L. and Coret, M. (2017) Elasticity and symmetry of tri-angular lattice materials. *International Journal of Solids and Structures*, 129 18–27.

Ganghoffer, J.F., Goda, I., Novotny, A.A., Rahouadj, R. and Sokolowski, J. (2018) Homogenized couple stress model of optimal auxetic microstructures computed by topology optimization. *ZAMM-Journal of Applied Mathematics and Mechanics/Zeitschrift für Angewandte Mathematik und Mechanik*, **98**(5) 696–717.

Ganghoffer, J.F. and Reda, H. (2021) A variational approach of homogenization of heterogeneous materials towards second gradient continua. *Mechanics of Materials*, 158 103743.

Giusti, S.M., Novotny, A.A., de Souza Neto, E.A. and Feijóo, R.A. (2009) Sensitivity of the macroscopic elasticity tensor to topological microstructural changes. *Journal of the Mechanics and Physics of Solids*, **57**(3) 555–570.

Greaves, G.N., Greer, A.L., Lakes, R.S. and Rouxel, T. (2011) Poisson's ratio and modern materials. *Nature Materials*, **10**(11) 823–837.

Lakes, R. (1993) Materials with structural hierarchy. *Nature*, **361**(6412) 511–515.

Liu, Z., Zhang, X., Mao, Y., Zhu, Y.Y., Yang, Z. Chan, C.T. and Sheng, P. (2000) Locally resonant sonic materials. *Science*, **289**(5485) 1734–1736.

Liu, Y. and Hu, H. (2010) A review on auxetic structures and polymeric materials. *Sci. Res. Essays,* **5**(10) 1052–1063.

Liu, Y. and Zhang, X. (2011) Metamaterials: a new frontier of science and technology. *Chemical Society Reviews*, **40**(5) 2494–2507.

Mánik, T. (2021) A natural vector/matrix notation applied in an efficient and robust return-mapping algorithm for advanced yield functions. *European Journal of Mechanics-A/Solids*, 90 104357.

Mehrabadi, M.M. and Cowin, S.C. (1990) Eigentensors of linear anisotropic elastic materials. *The Quarterly Journal of Mechanics and Applied Mathematics*, **43**(1) 15–41.

Mendez, C.G., Podestá, J.M., Toro, S., Huespe, A.E. and Oliver, X. (2019) *Making use of Symmetries in the 3D Elastic Inverse Homogenization Problem.* Begell House.

Novotny, A.A. and Sokolowski, J. (2012) *Topological Derivatives in Shape Optimization.* Springer Science & Business Media.

Novotny, A.A., Sokolowski, J. and Zochowski, A. (2019) *Applications of the Topological Derivative Method.* Springer, Cham, **188**.

Olympio, K.R. and Gandhi, F. (2010) Zero Poisson's ratio cellular honeycombs for flex skins undergoing one-dimensional morphing. *Journal of Intelligent Material Systems and Structures*, **21**(17) 1737–1753.

Peel, L.D. (2007) Exploration of high and negative Poisson's ratio elastomer-matrix laminates. *Physica Status Solidi (b)*, **244**(3) 988–1003.

Pironneau, O. (1984) *Optimal Shape Design for Elliptic Systems*. Springer-Verlag, New York.

Podestá, J.M., Mendez, C.M., Toro, S. and Huespe, A.E. (2019) Symmetry considerations for topology design in the elastic inverse homogenization problem. *Journal of the Mechanics and Physics of Solids*, 128 54–78.

Prawoto, Y. (2012) Seeing auxetic materials from the mechanics point of view: a structural review on the negative Poisson's ratio. *Computational Ma-terials Science*, 58 140–153.

Reese, S.P., Maas, S.A. and Weiss, J.A. (2010) Micromechanical models of helical superstructures in ligament and tendon fibers predict large Poisson's ratios. *Journal of Biomechanics*, **43**(7) 1394–1400.

Rossi, N., Yera, R., Mendez, C.G., Toro, S. and Huespe, A.E. (2020) Numerical technique for the 3D microarchitecture design of elastic composites inspired by crystal symmetries. *Computer Methods in Applied Mechanics and Engineering*, 359 112760.

Rossi, N., Podesta, J.M., Bre, F., Mendez, C.G. and Huespe, A.E. (2021) A microarchitecture design methodology to achieve extreme isotropic elastic properties of composites based on crystal symmetries. *Structural and Multidisciplinary Optimization*, **63**(5) 2459–2472.

Rychlewski, J. (1984) On Hooke's law. *Journal of Applied Mathematics and Mechanics*, **48**(3) 303–314.

Sigmund, O. and Maute, K. (2013) Topology optimization approaches: A comparative review. *Structural and Multidisciplinary Optimization*, **48**(6) 1031–1055.

Silverberg, J.L., Evans, A.A., McLeod, L., Hayward, R.C., Hull, T., Santangelo, C.D. and Cohen, I. (2014) Using origami design principles to fold reprogrammable mechanical metamaterials. *Science*, **345**(6197) 647–650.

Smith, D.R., Pendry, J.B. and Wiltshire, M.C.K. (2004) Metamaterials and negative refractive index. *Science*, **305**(5685) 788–792.

Sokolowski, J. and Zolésio, J.P. (1992) *Introduction to Shape Optimization*. Springer-Verlag, Berlin.

Sokolowski, J. and Zochowski, A. (1999) On the topological derivative in shape optimization. *SIAM Journal on Control and Optimization*, **37**(4) 1251–1272.

Spadoni, A. and Ruzzene, M. (2012) Elastostatic micropolar behavior of a chiral auxetic lattice. *Journal of the Mechanics and Physics of Solids*, **60**(1) 156–171.

Vianello, M. (1997) An integrity basis for plane elasticity tensors. *Archives of Mechanics*, **49**(1) 197–208.

Voigt, W. (1910) *Lehrbuch der Kristallphysik (mit ausschluss der Kristalloptik)*. BG Teubner, **34**.

Verchery, G. (1982) *Les invariants des tenseurs d'ordre 4 du type de l'élasticité*. In: J-P. Boehler, ed., *Mechanical Behavior of Anisotropic Solids /Comportement Mécanique des Solides Anisotropes*. Martinus Nijhoff Publishers & Editions du CNRS, 93–104.

Wang, P., Casadei, F., Shan, S., Weaver, J.C. and Bertoldi, K. (2014) Harnessing buckling to design tunable locally resonant acoustic metamaterials. *Physical Review Letters*, **113**(1) 014301.

Whitaker, S. (1985) A simple geometrical derivation of the spatial averaging theorem. *Chemical Engineering Education*, **19**(1) 18–52.

Whitaker, S. (2013) *The Method of Volume Averaging*. Springer Science & Business Media. **13**.

Yang, X.Y., Huang, X., Rong, J.H. and Xie, Y.M. (2013) Design of 3D orthotropic materials with prescribed ratios for effective Young's moduli. *Computational Materials Science*, **67** 229–237.

Yera, R., Rossi, N., Mendez, C.G. and Huespe, A.E. (2020) Topology design of 2D and 3D elastic material microarchitectures with crystal symmetries displaying isotropic properties close to their theoretical limits. *Applied Materials Today*, 18 100456.